Journal of
Synchrotron
Radiation

ISSN 1600-5775

Received 25 June 2013
Accepted 11 September 2013

Study of fossil bones by synchrotron radiation micro-spectroscopic techniques and scanning electron microscopy

I. M. Zougrou,[a] M. Katsikini,[a]* F. Pinakidou,[a] E. C. Paloura,[a] L. Papadopoulou[b] and E. Tsoukala[b]

[a]School of Physics, Aristotle University of Thessaloniki, 54124 Thessaloniki, Greece, and [b]School of Geology, Aristotle University of Thessaloniki, 54124 Thessaloniki, Greece. *E-mail: katsiki@auth.gr

Earlymost Villafranchian fossil bones of an artiodactyl and a perissodactyl from the Milia excavation site in Grevena, Greece, were studied in order to evaluate diagenetic effects. Optical microscopy revealed the different bone types (fibro-lamellar and Haversian, respectively) of the two fragments and their good preservation state. The spatial distribution of bone apatite and soil-originating elements was studied using micro-X-ray fluorescence (μ-XRF) mapping and scanning electron microscopy. The approximate value of the Ca/P ratio was 2.2, as determined from scanning electron microscopy measurements. Bacterial boring was detected close to the periosteal region and Fe bearing oxides were found to fill bone cavities, *e.g.* Haversian canals and osteocyte lacunae. In the perissodactyl bone considerable amounts of Mn were detected close to cracks (the Mn/Fe weight ratio takes values up to 3.5). Goethite and pyrite were detected in both samples by means of metallographic microscopy. The local Ca/P ratio determined with μ-XRF varied significantly in metal-poor spots indicating spatial inhomogeneities in the ionic substitutions. XRF line scans that span the bone cross sections revealed that Fe and Mn contaminate the bones from both the periosteum and medullar cavity and aggregate around local maxima. The formation of goethite, irrespective of the local Fe concentration, was verified by the Fe *K*-edge X-ray absorption fine structure (XAFS) spectra. Finally, Sr *K*-edge extended XAFS (EXAFS) revealed that Sr substitutes for Ca in bone apatite without obvious preference to the Ca_1 or Ca_2 unit-cell site occupation.

Keywords: XRF imaging; XAFS; SEM; fossil bones; apatite.

1. Introduction

Skeletal parts, which are often the only fossil remains, are very important paleontological findings since they provide valuable information on the evolution of living organisms, the palaeo-climate and palaeoenviroment (*e.g.* Gingerich, 1984; Sasowsky & Mylroie, 2007; Sheldon & Tabor, 2009). Bones are composite materials composed of nanometer-sized bioapatite crystals and other phosphate minerals embedded in an organic matrix consisting mainly of type I collagen (Wopenka & Pasteris, 2005; Collins *et al.*, 2002). The structure of compact bone is described on two levels: on the basis of the collagen fibre orientation, mammalian bones are categorized into four types of primary bone: (*a*) woven bone is a fast-deposited type of usually fetal bones that is characterized by randomly oriented collagen fibres and large osteocyte lacunae; (*b*) lamellar bone is a mature bone grown at slow rates where the well oriented collagen fibrils are arranged in sheets (lamellae). The osteocyte lacunae are typically flatter and more evenly distributed than in woven bone; (*c*) parallel fibered bone is an intermediate type of bone where the collagen fibres are oriented parallel to the surface; (*d*) fibro-lamellar bone is formed when spaces in woven or parallel-fibered bone are covered by lamellar bone formed around vascular canals, resulting in the creation of primary osteons inside the woven bone (Currey, 2002). Based on the type of vascularization, Enlow & Brown (1956), de Ricqles (1975) and de Ricqles *et al.* (1991) classified the vascular patterns of compact bone into four categories: (*a*) non-vascular bone tissue; (*b*) primary vascular canals oriented in one direction (longitudinal, radial, circular, oblique vascular canals); (*c*) primary vascular canals oriented in more than one direction (laminar, plexiform, reticular vascular canals); (*d*) bone tissue secondary vascular canals composed of secondary osteons (Haversian systems). The secondary osteons are formed by osteoclastic resorption of older lamellae leading to an enlargement of the vascular canal and subsequent osteoblastic deposition of circumferential lamellae. This process is known as secondary remodelling. Angular intervals of

remnant old lamellar bone found between new adjacent secondary osteons are called interstitial lamellae. The secondary osteons are distinguished from the primary ones by the cement lines surrounding their boundaries (Currey, 2002).

The histological features of palaeontological bone are subjected to diagenetic changes which are strongly affected by the burial environment. Bone alterations, such as bioerosion borings (Wedl, 1864; Hackett, 1981; Child, 1995; Marchiafava *et al.*, 1974), destruction of primary bone and cracks induced by the fossilization process, can be investigated at the microscopic level using optical microscopy. Pfretzschner (2004) described two stages of diagenetic alteration resulting in bone fossilization. During the early diagenetic stage microbial degradation, gelatinization and replacement of collagen by apatite and other phases occur. Mineral precipitation at this stage is controlled by high pH values and low redox conditions and is restricted to Haversian canals, osteocyte lacunae and cement lines. Pyrite formation during early diagenesis originates from collagen decaying sulfide released in water. The late diagenesis stage starts after the full replacement of collagen and is controlled by environmental conditions. The minerals precipitating at this stage replace apatite in the structure or fill cracks propagating through the structure. In order to assess the degree of diagenetic alterations in archaeological Haversian bones, Hedges *et al.* (1995) proposed the use of the Oxford Histological Index (OHI) that scales from 5 (very well preserved bone) to 0 (badly preserved histology) according to characteristics observed in light microscopy images. Collagen loss and alterations in crystallite properties of the apatite mineral can be studied by synchrotron radiation small-angle X-ray scattering and infrared spectroscopy (Hiller & Wess, 2006; Wess *et al.*, 2001; Lebon *et al.*, 2011; Reiche *et al.*, 2010) while synchrotron radiation micro-tomography may be used to access non-destructively the inner structural morphology (Mazurier *et al.*, 2006). The chemical alterations of the bone, as for example the incorporation of soil-originating elements, can be studied using chemical mapping techniques. More specifically, spatially resolved quantitative information at the micrometer scale can be obtained with scanning electron microscopy (SEM) and micro X-ray fluorescence (μ-XRF) mapping. The former requires special sample preparation, it is surface sensitive and suffers from low sensitivity for high-Z elements while the latter is non-destructive, provides good spatial resolution and offers high sensitivity to elements with $Z > 13$ (Dumont *et al.*, 2009). The μ-XRF mapping in combination with micro-X-ray absorption fine structure (μ-XAFS) spectroscopy offer a valuable tool for the spatially resolved quantitative information and speciation of various intra- or exogenous elements.

Fresh bone apatite has been identified as B-type carbonated hydroxylapatite with composition $Ca_{10-x}[(PO_4)_{6-2x}(CO_3)_{2x}](OH)_2$ (Wopenka & Pasteris, 2005). However, during fossilization, bioapatite is chemically and structurally modified due to the uptake of soil-originating elements and recrystallization (Pfretzschner, 2004). Carbonated fluorapatite has been identified as the main constituent of fossil bone apatite (Gruner & McConnell, 1937; Newesely, 1989; Frank-Kamenetskaya, 2008). Apatite is very susceptible to ionic substitutions (Skinner, 2005; Pasero *et al.*, 2010; Tamm & Peld, 2006). One of the elements that substitute for Ca, which has also been used in osteoporosis treatment studies, is strontium (Boivin *et al.*, 1996; Rochefort *et al.*, 2010; Roschger *et al.*, 2010). In the unit cell of apatite, two non-equivalent Ca sites exist, denoted as Ca_1 and Ca_2 (Mehmel, 1930). Various theoretical and experimental studies have been conducted on the preferred location of Sr in the two Ca sites with contradicting results (Terra *et al.*, 2009; Li *et al.*, 2007; Bigi *et al.*, 2007; Hughes *et al.*, 1991). However, studies on the local environment of Sr incorporated in fossil bones are scarce.

In this study we investigate fossil bones of Earlymost Villafranchian (MNQ 16) excavated at the Milia site in Grevena, Greece. Bone fragments of an artiodactyl and a perissodactyl were selected as representative of small and large mammal specimens of the local fauna because of their different bone histology. Although the bone type may vary even within bones of the same individual, the order of artiodactyla is typically comprised of plexiform bone in the outer layers of compact bone and secondary osteons in the middle and inner layers (Enlow & Brown, 1958; Martiniakovà *et al.*, 2006). The perissodactyla order may be comprised of fibrolamellar (reticular or plexiform) bone with areas of isolated or dense secondary osteons (Enlow & Brown, 1958; Cuijpers, 2006). Larger mammal bone of the proboscidea order is constituted from laminar fibrolamellar bone and secondary osteons (Curtin *et al.*, 2012; Rogoz *et al.*, 2012). It has been suggested that smaller bones are considered to be more susceptible to diagenetic alterations (Nicholson, 1996; Von Endt & Ortner, 1984; Behrensmeyer *et al.*, 1979). The histological evaluation and the spatial distribution of elements were studied by transmitted light microscopy, SEM and synchrotron radiation (SR) μ-XRF spectroscopy. The speciation of Sr and thus the possible Ca site preference in bone apatite was investigated by means of Sr *K*-edge extended-XAFS (EXAFS) spectroscopy. The local bonding environment of Fe, a common soil contaminant in fossil specimens, was determined by μ-XAFS. The X-ray absorption near-edge structure (XANES) portion of the Fe *K*-edge XAFS spectra is very sensitive to its bonding configuration (ligation and geometry) and oxidation state (Westre *et al.*, 1997). More specifically, the characteristic pre-edge peak that appears below the Fe *K* absorption edge is related to $1s \rightarrow 3d$ transitions that become dipole allowed due to mixing of the $3d$ with the $4p$ orbitals and provides information on the oxidation state of Fe and the type of the polyhedra it forms. Further information on the bonding configuration of Fe is obtained by the shell-by-shell fitting of the EXAFS spectrum that reveals the nearest-neighbour distances, the coordination numbers and the extent of the thermal and static disorder.

2. Materials and methods

The studied samples are Earlymost Villafranchian (MNQ 16) fossil bone fragments of an artiodactyl (possibly *sus*), named

MIL5-780, and a perissodactyl (*rhinoceros*), named MIL5-743, excavated at the terrestrial depositional environment of Milia (site MIL5), in Grevena, Greece (Tsoukala, 2000). The bones were found at a depth of approximately 15 m and thus were protected from periodic fluctuations of temperature and humidity occurring at the surface. Their colour is yellowish (MIL5-780) and brownish (MIL5-743), respectively. The fossil record of large mammals dating from this stage is scarce in Greece and most of the European continent. However, in the Milia site a vast number of mammal bone and teeth were preserved including *Mammut borsoni*, *Anancus arvernensis*, *Elephas antiquus* and other species. The wider basin of Grevena is situated near Mount Pindos and Aliakmon River. The Pliocene–Quaternary deposits of the Grevena basin, in which the fossils were found, consist of Pliocene lacustrine deposits, followed by a Plio-Pleistocene sequence of clastic deposits, mainly sands, gravels and conglomerates, with sandstone intercalation and silty lenses (Tsoukala & Lister, 1998).

Transmitted light microscopy was used for the identification of the bone histology and the evaluation of the diagenetic alterations. Reflected light metallographic microscopy was used for the identification of metal structures. For this purpose the samples were prepared according to the procedure followed by Hedges *et al.* (1995). More specifically, the bones were impregnated in epoxy resin, set in a vacuum chamber for 5 min and left to cure at room temperature for one day. Then they were cut into transverse sections that included the periosteal surface. More specifically, the dimensions of the transverse section from the perissodactyl were about 4 cm across and 1.5 cm thick, while those from the artiodactyl section were 2 cm across and 0.5 cm thick. Finally, the sections were initially ground using 400–800 SiC grit papers and then polished with diamond paste with grain diameter 6 and 3 µm sequentially, until their thickness was 0.5 mm. The SEM characterization was performed using a Jeol JSM-840A scanning electron microscope equipped with an energy-dispersive X-ray spectrometer (EDS) operating at 20 kV accelerating voltage and 0.4 mA probe current in the back-scattering electron (BSE) analysis mode. Pure Co was used as an optimization element and a standard for the analyses of the mineral phases (registered standard number 1773, Micro-Analysis Consultants Ltd). Prior to the SEM characterization, a thin (20 nm) carbon coating was deposited on the sample surface in order to render them electrically conductive.

The SR-XRF and µ-XAFS measurements were conducted at the BESSY II synchrotron radiation storage ring of the Helmholtz Zentrum Berlin. The measurements were performed at the KMC-II beamline at atmospheric pressure using an energy-dispersive fluorescence (XFlash-Röntec) silicon detector positioned on the horizontal plane at right angles to the incident beam. The total flux at the sample spot was in the range 10^9–10^{10} photons s^{-1} (Bartoll *et al.*, 2004). The beam was focused using a circular capillary that reduced the beam size to 3.6 µm. The one-dimensional (line scans) and two-dimensional SR-XRF maps were recorded using a beam with excitation energy of 9.7 and 7.2 keV, respectively, impinging at 45° to the sample surface. For the construction of the XRF maps, the integrated count rate of the $K\alpha$ emission peak of the corresponding element was taken into account [range-of-interest (ROI) integration]. The macro-XAFS measurements (beam size 6 mm × 1 mm) were conducted at the C beamline of the DORIS storage ring at HASYLAB using a seven-element fluorescence detector. The photon flux on the sample was 10^9 photons s^{-1}. For the XRF and XAFS spectra the samples were cut into transverse sections that included the periosteal surface and then they were cleaned, air-dried and ground with 400–800 SiC grit papers. The measurements were recorded on the cross sections of the bulk samples.

For the quantitative analysis of the µ-XRF spectra, they were fitted using the *WinQXAS* package (Vekemans *et al.*, 1994), taking into account corrections for escape peaks. The weight ratio C_A/C_B for elements A and B was determined using the equation (Janssens *et al.*, 2000)

$$\frac{C_A}{C_B} = \frac{R_{Ajk}}{R_{Bjk}} \frac{Y_{Bjk}}{Y_{Ajk}} \frac{S_{Bjk}}{S_{Ajk}}, \tag{1}$$

where

$$Y_{ijk} = \frac{\Omega}{4\pi} \varepsilon\left(E_{ijk}\right) \omega_{ij}\, p_{ijk}\, \tau_{ij}(E_0) I_0(E_0), \tag{2}$$

$$S_{ijk} = 1 \Big/ \left[\frac{\mu(E_0)}{\sin\theta} + \frac{\mu(E_{ijk})}{\sin\varphi}\right] \rho d \qquad (i = A, B). \tag{3}$$

R_{ijk} is the area under the corresponding peak in the XRF spectrum, the term Y_{ijk} includes the element-specific cross sections and the term S_{ijk} accounts for self-absorption corrections taking into account the irradiated mass of the sample (ρd) and is important in the case of thick and/or concentrated samples. j denotes the shell where the core due to absorption is formed and k the specific transition line (*e.g.* $K_{\alpha 1}$: $L_3 \rightarrow K$ transition), Ω is the detector solid angle, ε is the detector's efficiency at the fluorescence energy E_{ijk} of the specific element, ω_{ij} is the fluorescence yield, p_{ijk} is the transition probability of the kth line of the element i, τ_{ij} is the subshell photoelectric cross section and I_0 is the intensity of the impinging beam (Bandyopadhyay & Segre, undated; Ravel & Newville, 2005). $\mu(E_0)$ and $\mu(E_{ijk})$ are the mass absorption coefficients of the sample at the excitation and fluorescence energies and θ and φ are the angle of incidence and detection, respectively. The mass absorption coefficients, $\mu(E_0)$ and $\mu(E_{ijk})$, of the matrix were calculated using the composition of the corresponding sample region determined from the SEM–EDX maps in regions where a small amount of Fe was detected and FeOOH in Fe-rich sample spots. This assumption is used as an approximation of the average sample composition determined by SR-XRF. The penetration depth of the primary electron beam in SEM–EDX measurements is a few micrometres while in the SR-XRF spectra the excitation depth for hydroxylapatite is 63 µm. However, self-absorption effects induced by elements dominating the sample (Ca, P) result in an information depth of approximately 12 µm for an excitation energy of 9.7 keV. Although the histological

features in bone gradually vary along the axial direction and consequently the local elemental composition may change, the SR-XRF information depth is not as high as to give completely different compositional information but can rather be used as a prompt tool of the average composition in a finite volume near the surface. The analysis of the EXAFS spectra was conducted using the *FEFF8* package (Ankudinov *et al.*, 1998; Newville *et al.*, 1995). The XANES spectra were subjected to linear background subtraction and normalization to the edge jump and the fitting of the isolated pre-edge peak was performed with the *PeakFit* software.

3. Results and discussion

3.1. Optical microscopy

The transmitted light images of the perissodactyl and the artiodactyl bone are shown in Figs. 1(*a*, *b*) and 1(*c*, *d*), respectively. The images reveal the different typology of the two bone tissues. The compact bone of the perissodactyl is characterized by a well preserved secondary osteon (Haversian system) structure. Many histological features such as the Haversian canals, the circumferential lamellate structure and the osteocyte lacunae have been preserved and thus an OHI equal to 3 was assigned. Various resorption cavities (marked with 'Res') denoting remodelling processes for secondary bone deposition are also observed. The average diameter of the Haversian canals is 31.1 ± 1.8 μm and their mean distance is 111 ± 6 μm. Contrary to the perissodactyl bone, the artiodactyl bone consists of reticular fibro-lamellar tissue with primary osteons arranged in a laminar to plexiform pattern. Transverse vascular canals, with thickness that is progressively reduced from the periosteum to the endosteum, separate the bone tissue in approximately 200 μm-thick layers. Secondary remodelling is also observed near the periosteum area. As in the case of the perissodactyl bone, an OHI equal to 3 was assigned to the artiodactyl bone due to the preservation of lamellate structure and the visibility of osteocyte lacunae in the primary and secondary osteons. The average diameter of the primary longitudinal canals is 40.3 ± 1.8 μm. Diagenetic effects are evident in both samples in the form of cracks that propagate through the bone histology.

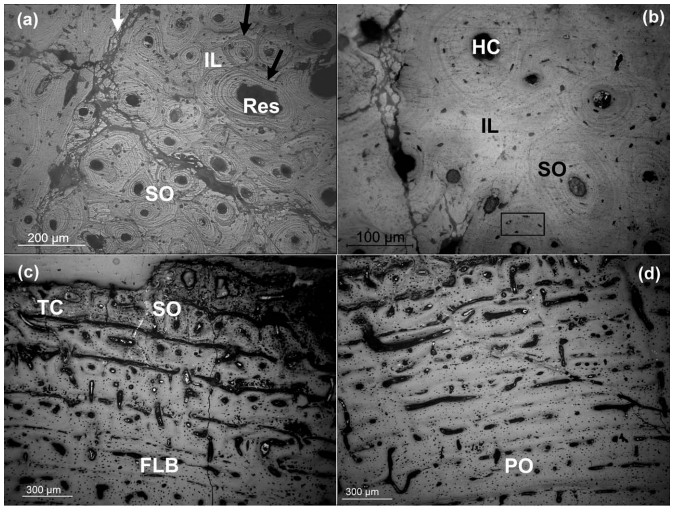

Figure 1
Transverse sections of cortical bone of the perissodactyl (*a*, *b*) and artiodactyl (*c*, *d*) samples viewed under transmitted light. The perissodactyl bone is characterized by a Haversian-type histology. Some cement lines are indicated with black arrows whereas a diagenetic crack is denoted by a white arrow in (*a*). Well preserved osteocyte lacunae are indicated with a black rectangular in (*b*). The artiodactyl bone has a characteristic fibro-lamellar structure with primary osteons. Remodelling in the periosteum area is evident in (*c*). Notation: SO, secondary osteons (Haversian systems); IL, interstitial lamellae; Res, resorption cavity; HC, Haversian canal; FLB, fibro-lamellar bone; PO, primary osteons; TC, transverse vascular canal.

Reflected light images were used for the identification of metallic phases and alloys. Pyrite and goethite were detected in both samples from the periosteum to the cancellous bone, with the extent of the latter being considerably larger in both samples compared with pyrite. The pyrite formation appears to have occurred before goethite, as many Haversian canals and resorption cavities are filled with pyrite in the centre while goethite is deposited in the perimeter or the outer areas. Based on histological evidence the pyrite formation occurred both during early and late diagenetic stages. Pyrite formed at this early stage was observed filling Haversian and vascular canals as well as some osteocyte lacunae without affecting general histological features. Early diagenesis pyrite is more prominent in the artiodactyl bone. Pyrite precipitated during late diagenesis was detected in diagenetic cracks propagating through the histology, around the perimeter or partially replacing resorption cavities as well as in various spaces of the trabecular bone. The formation of pyrite during late diagenesis indicates high pH values which are also necessary for the formation of goethite. The sulfide necessary for the precipitation of pyrite at this stage originates from the fluvial Plio-pleistocene formation in which the fossils were found.

3.2. Scanning electron microscopy

The spatial distribution of bone and soil-originating elements was studied by means of SEM. The SEM–BSE images of the artiodactyl and perissodactyl bones are shown in Figs. 2 and 3, respectively. Cracks and chemical alterations in the form of unmineralized areas (holes) up to 60 μm wide and various hypermineralized areas can be easily distinguished. Extensive bacterial boring reaching up to 300 μm from the periosteum was detected in the artiodactyl bone. The borings have a mean diameter of 8 μm and are filled with spherical nodules (Fig. 2*a*). The SEM–EDX maps of the artiodactyl bone recorded at the cortical bone (Fig. 2*b*) are shown at the bottom of Fig. 2. It can be clearly seen that the spatial distribution of Ca and P is similar indicating their co-participation in the formation of the bone apatite (marked as CaP). The Ca/P weight ratio in compact bone, as determined by the various SEM–EDX maps, is approximately 2.2. The standard deviation in the Ca/P ratios is 7% (±0.16). These values are close to the theoretical value of 2.15 determined for fresh bone (White & Hannus, 1983). Indeed, ratios in the range 2.07–2.20 have

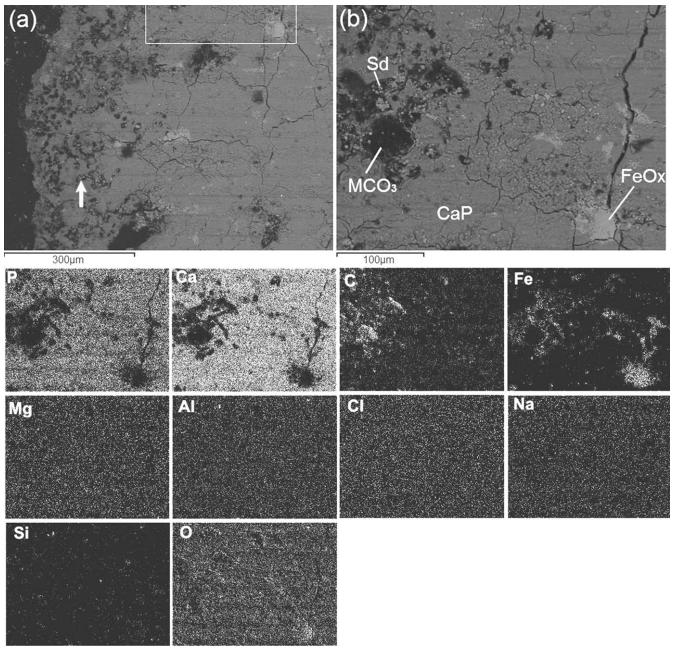

Figure 2
(*a*) SEM–BSE image acquired near the periosteal area in the artiodactyl bone cross section. Bright areas are rich in heavier elements compared with the darker ones. The arrow indicates the extensive microbial tunneling that appears in the form of spherical nodules. The inset denotes part of the area where SEM–EDX maps were recorded. (*b*) SEM–BSE image and corresponding SEM–EDX maps (bottom) recorded at approximately 0.6 mm from the periosteum. Notation: FeO_x, Fe (hydroxy)oxides; Sd, siderite ($FeCO_3$); CaP, apatite; MCO_3, carbonate mineral.

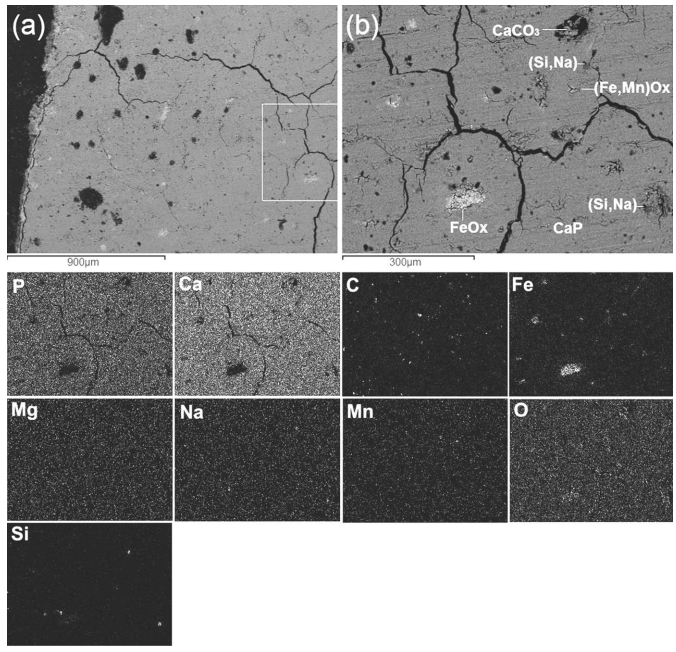

Figure 3
(*a*) SEM–BSE image acquired at the periosteal area of the perissodactyl bone cross section. The inset denotes part of the area where the SEM–EDX maps were recorded. (*b*) SEM–BSE image and corresponding SEM–EDX elemental maps (bottom) recorded at approximately 1.2 mm from the periosteum. Fe (hydroxy)oxide precipitates fill Haversian canals (Fe, O maps). A small Mn contribution was detected in a Fe-rich precipitate (Mn map) while Si and Na form small precipitates near holes (Si, Na maps). Notation: FeO_x, Fe (hydroxy)oxides; Si, Na, (Si, Na) mineral; CaP, apatite; $CaCO_3$, calcite.

been reported (Elliott *et al.*, 2002). The detected metal-rich phases are mainly Fe-bearing oxides. Fe (hydroxy)oxides, marked as FeO_x in the BSE image, fill voids, and aggregate preferably close to cracks. Indeed, goethite filling Haversian canals and osteocyte lacunae throughout the samples' cross sections was detected by means of metallographic microscopy. Pyrite was also detected in osteocyte lacunae and partially filling vascular canals. Furthermore, sphericules of siderite ($FeCO_3$), marked as Sd, are also detected by EDX spot analysis inside the cavities and could be attributed to early microbial activity (Clarke, 1994; Elorza *et al.*, 1999). The Fe/Ca and Mn/Ca weight ratios detected in various SEM–EDX maps of areas covered only with secondary osteons were approximately 0.036 ± 0.0025 and $(3.52 \pm 0.25) \times 10^{-3}$, respectively. Other phases appearing from the EDX maps were: (*a*) carbonate minerals (marked as MCO_3) other than $CaCO_3$, $FeCO_3$, $MgCO_3$, possibly witherite ($BaCO_3$) which is a common void-filling mineral, appear to fill other cavities; (*b*) small Si-rich spots appear throughout the sample and might correspond to SiO_2 and/or as some aluminosilicate mineral (Si, O, Al maps). Contrary to Fe, Si and Al, that clearly originate from the burial environment, Mg, Cl and Na can both have an endogenous and exogenous origin.

In the SEM–BSE image of the perissodactyl bone shown in Fig. 3(*a*), the destruction was limited much closer to the periosteal region. Furthermore, most of the primary bone near the periosteum is strongly enriched in metal-rich phases. Pyrite and goethite were also observed by means of metallographic microscopy. The presence of pyrite in the compact bone of this sample is restricted mainly to diagenetic cracks and to a lesser extent in partially filling Haversian canals. Magnification of the area indicated by the white rectangle is shown in Fig. 3(*b*). The corresponding SEM–EDX maps are shown at the bottom of Fig. 3. The apatite location can be clearly distinguished along with the characteristic Haversian canals. The average Ca/P ratio is found equal to 2.2 in both the periosteal and cortical regions from the EDX maps. Most of the Haversian canals are filled with Fe-bearing oxides whereas in others the contribution of Mn is also detected [indicated as $(Fe,Mn)O_x$]. Fe- and Mn-rich oxides precipitate also along bone cracks. The Mn/Fe weight ratio determined from the SEM–EDX measurements takes values up to 0.14 in the periosteal area. However, in the cortical region, the average Mn/Fe weight ratio in areas containing mainly apatite took values up to 0.45 while in Mn-rich (hydroxy)oxide phases that precipitate near bone cracks the local Mn/Fe molar ratio takes values up to 3.6. Presumably, Fe was disposed in an earlier diagenetic stage filling bone voids, while Mn has been introduced at a later stage, perhaps after the formation of cracks which opened new diffusion paths. Small Si- and Na-rich precipitates probably originating from the sediment [denoted as (Si, Na)] are located near holes.

Table 1
Elements detected with SR-μ-XRF spectroscopy at the cross section of the artiodactyl bone and corresponding elemental weight ratios.

The spectra were recorded at spots of the compact bone (CB) and periosteum (P) areas which are indicated in Fig. 4. Fe-rich and Fe-poor designate the spots where μ-XAFS measurements were conducted. The main detected phases are also listed. The elemental weight ratios were corrected for self-absorption using either a FeOOH matrix in the Fe-rich regions or the elemental concentration obtained from the SEM–EDX maps in apatite-rich regions.

Spectrum	Detected elements	Main detected phases	Ca/P	Fe/Ca	Mn/Ca ($\times 10^{-3}$)	Zn/Ca ($\times 10^{-3}$)
xrf1 (CB)	P, Ca, Mn, Fe, Zn	Apatite	3.5	0.09	5.7	2.2
xrf2 (CB)	Ca, Fe, Cu, Zn	Metal-rich oxides	–	0.52	12.9	210
xrf3 (CB)	P, Ca, Mn, Fe, Zn	Apatite	1.84	0.09	5.5	1.9
xrf4 (CB)	P, Ca, Fe, Zn	Apatite, metal-rich oxides	1.84	0.52	3.1	2.2
xrf5 (CB)	P, Ca, Fe	Metal-rich oxides	1.11	1.49	3.4	5.8
xrf6 (CB)	P, Ca, Fe, Zn	Metal-rich oxides	1.2	1.9	3.4	7.8
xrf7 (P)	P, Ca, Mn, Fe	Apatite	3.37	0.06	5.6	–
xrf8 (P)	P, Ca, Mn, Fe	Apatite	2.4	0.14	4.7	–
xrf9 (P)	P, Ca, Mn, Fe	Apatite	2.95	0.06	6.1	–
xrf10 (P) (Fe-rich)	P, Ca, Fe	Metal-rich oxides	1.48	2.3	–	–
xrf11 (P) (Fe-poor)	P, Ca, Mn, Fe	Apatite	2.12	0.05	4.4	–

3.3. SR-XRF spectroscopy and mapping

The local chemical changes, which are mainly related to soil-originating elements, are studied using μ-XRF spectra recorded at selected spots (denoted as xrf1–11) of the artiodactyl bone cross section (Fig. 4*a*). Representative μ-XRF spectra recorded at the periosteum and compact bone regions are shown in Fig. 4(*b*). The detected elements and their weight ratios are listed in Table 1. The concentration of Mn, Fe, Cu and Zn is found to vary considerably revealing the precipitation of metal-rich phases that originate from the burial environment. Zn in trace-element concentrations has been proposed as an element useful for dietary reconstruction in prehistoric bones (Gilbert, 1975). Guggenheim & Gaster (1973) reported that Zn levels in modern adult human bones remain unaltered, while Lambert *et al.* (1979, 1982, 1984, 1985) and Beck (1985) suggested that Zn in archaeological bone is not affected by diagenetic processes. Safont *et al.* (1998) reported that Zn in fossil bones can be used to discriminate herbivorous from carnivorous animals. Various studies use Zn as a paleodietary indicator (Schutkowski *et al.*, 1999; İzci *et al.*, 2013; White & Schwarcz, 1989); however, its validity has been questioned (Ezzo, 1994*a*,*b*). The local maximum of the Zn concentration that was identified with the xrf2 spectrum cannot (due to its extreme value) be attributed to pre-mortem Zn incorporation in the apatite structure but instead should be attributed to soil contamination. The Ca/P ratio is found to range from 1.8 to 3.5 in the various spots which are poor in Mn and Fe. The presence of transition metals even in small concentrations in the probed volume increases the information depth of fluorescence photons. The lower Fe/Ca ratio observed is 0.05 which is close to the 0.04 value of SEM–EDX maps corresponding to Fe filling Haversian canals and osteocyte lacunae in areas of compact bone covered only with secondary osteons. The Ca/P weight ratio determined by SR-XRF is 2.12, which is (within the error limits) in agreement with the SEM measurements (2.2 ± 0.16). The Mn/Ca ratio is 4.4×10^{-3}, while the respective SEM weight ratio is $(3.5 \pm 0.25) \times 10^{-3}$. In Fe-rich spots (with Fe/Ca = 0.06) the Ca/P weight ratio value is increased to approximately 3, depicting the influence of metals when probing a bulk sample. Consequently, SR-XRF measurements in well preserved bulk compact secondary osteons bone could be used to detect elemental ratios provided the metallic element concentration is low (*i.e.* distant to areas with diagenetic cracks that are usually filled with metallic precipitations).

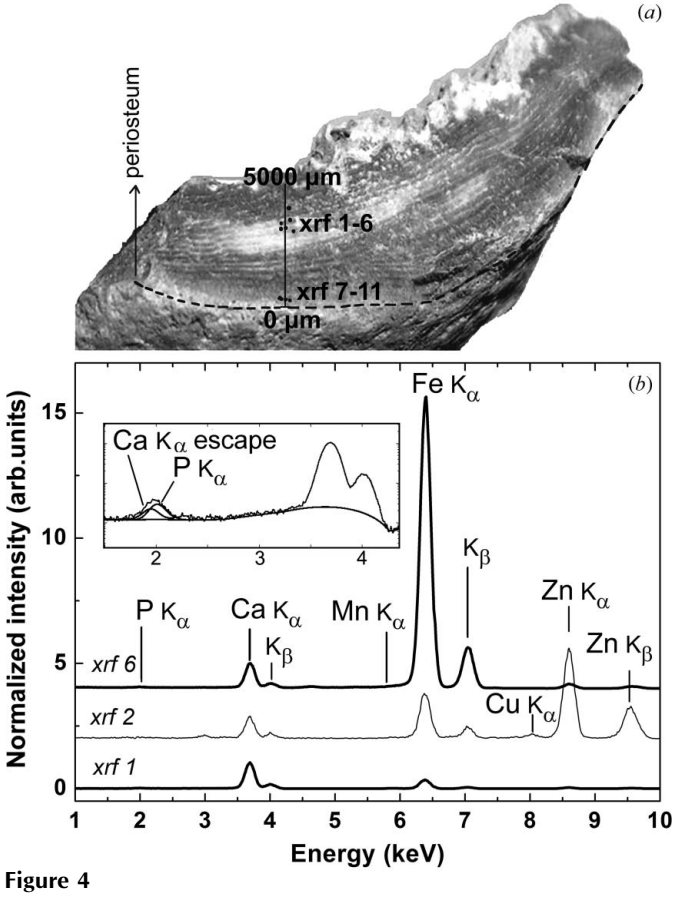

Figure 4
(*a*) Photograph of the cross section of the artiodactyl bone. The spots indicate the positions where μ-XRF spectra were recorded. (*b*) Representative μ-XRF spectra. The contribution of the Ca *Kα* escape peak near the P *Kα* peak is shown in the inset.

The paths of soil element contamination were investigated using μ-XRF line-scans (one-dimensional maps) that span the cross section of the bone. The shape of the concentration profile of each element provides information on the paths of bone alteration (Rousseau, 1984; Wings, 2004). The line-scans of P, Ca, Mn and Fe $K\alpha$ emission intensities from the periosteal to the trabecular region of the artiodactyl bone are shown in Fig. 5(*a*). The corresponding scan for the perissodactyl bone is shown in Fig. 5(*b*). In order to account for the different emission and absorption probabilities of the various elements, their profiles were normalized by $\varepsilon(E_{ijk})\,\omega_{ij}\,p_{ijk}\,\tau_{ij}(E_0)$ and the detector-to-sample air-path absorption. The distribution profiles shown in Fig. 5 reveal that: (i) Ca and P have an almost constant intensity in the cortical area whereas the Ca distribution exhibits local maxima in the trabecular bone due to increased porosity and possible precipitation of secondary minerals; (ii) the distribution of Fe is inhomogeneous exhibiting a number of local maxima. The higher density of the Fe-maxima at the edges of the bone's cross section indicates that the contamination originated from both the periosteum and the medullar cavity *via* diffusion or recharge processes; (iii) Mn shows also an irregular profile although its concentration is much lower compared with that of Fe especially in the perissodactyl bone.

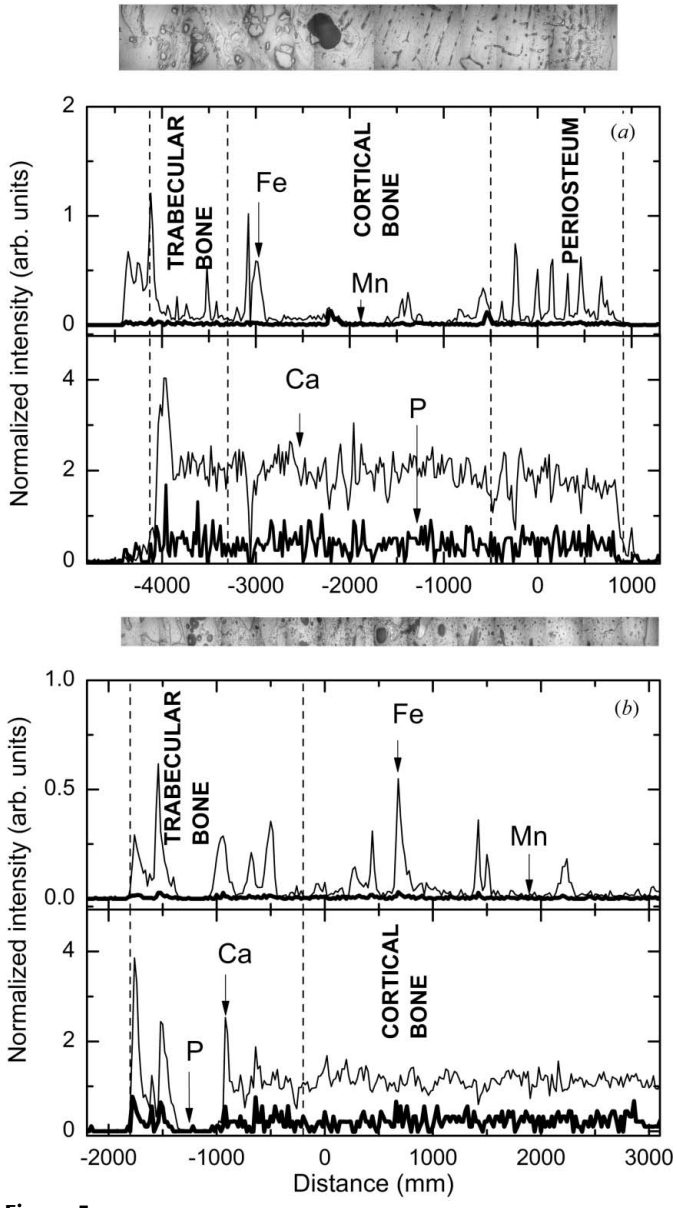

Figure 5
μ-XRF line-scans of P, Ca, Fe and Mn recorded along the cross section of the (*a*) artiodactyl and (*b*) perissodactyl bone. The count rate that corresponds to each element is selected using proper energy windows in the XRF spectra and was normalized by $\varepsilon(E_{ijk})\,\omega_{ij}\,p_{ijk}\,\tau_{ij}(E_0)$. The absorption of the sample-to-detector air path was also taken into account.

The two-dimensional SR-XRF elemental maps of the artiodactyl (fibrolamelar) bone that were recorded in the cortical area at approximately 3.0 mm from the periosteum are shown in Fig. 6. The interpretation of the detected features is based on the vascular types and bone tissue observed in the transmitted light microscopy images of the sample. Areas of minimum Ca and P intensity are attributed, according to their shape, to longitudinal, radial and reticular vascular canals. Two radial canals (denoted as 1, 2) with dimensions 25 × 47 and 23 × 42 ± 2.5 μm, four longitudinal canals (3–6) with diameters of 50, 30, 30 and 25 ± 2.5 μm and a reticular canal (7) are detected. The diameter of most longitudinal canals observed in the maps is in agreement with the average primary osteon canal diameter (31 μm) identified in the optical microscopy images (see Fig. 1). The Ca and P concentrations are increased around the canal boundaries (more profound in the Ca maps) while Fe and Mn fill voids and/or canals. The two-dimensional SR-XRF elemental maps of the perissodactyl (Haversian) bone, which were recorded in its cortical area at approximately 5 mm from the periosteum, are shown in Fig. 7. The following features can be identified in the maps: a

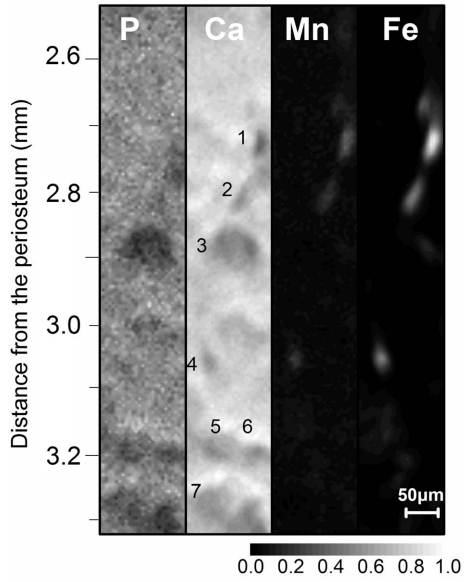

Figure 6
SR-XRF maps of the sample of the artiodactyl bone recorded at compact fibrolamellar bone at a distance of approximately 2.5 mm from the periosteum. The incident beam impinges at 45° to the sample surface. The detector is positioned at right angles to the beam. The map of each element is normalized jointly with the corresponding map in Fig. 7 to the maximum of the element.

Table 2
Fitting results of the Sr *K*-edge macro-EXAFS spectra recorded at the cross section of the artiodactyl and the perissodactyl bones.

N is the coordination number, *R* is the nearest-neighbour distance from the Fe absorbing atom, σ^2 is the Debye–Waller factor. During the iterations the value of *N* was kept fixed according to the fluorapatite model.

		Nearest-neighbouring shells					
Specimen	Parameters	SH1: O	SH2: P	SH3: Ca	SH4: Ca	SH5: O	SH6: O
Artiodactyl bone	*N*	7.2	2.4	0.8	7.2	4.2	
	R (Å)	2.49 ± 0.01	3.17 ± 0.04	3.47 ± 0.04	4.05 ± 0.02	4.45 ± 0.04	
	$\sigma^2 \times 10^{-2}$ (Å^2)	1.1	2.2	2.2	2.2	1.5	
Perissodactyl bone	*N*	7.2	2.4	0.8	7.2	4.2	6.6
	R (Å)	2.52 ± 0.01	3.21 ± 0.01	3.47 ± 0.02	4.13 ± 0.05	4.43 ± 0.04	4.92 ± 0.04
	$\sigma^2 \times 10^{-2}$ (Å^2)	1.2	1.7	0.64	2.8	0.3	0.5
Fluorapatite model (Hughes *et al.*, 1989)	*N*	7.2	2.4	0.8	7.2	4.2	6.6
	R (Å)	2.51	3.19	3.44	4.03	4.44	4.80

secondary osteon located at 4.7 mm with Haversian canal (marked with '1') of diameter 37.5 ± 4 µm, an osteocyte lacuna (marked with '2') of diameter 10 ± 2.5 µm and part of a resorption cavity (marked with '3') of length 290 ± 2.5 µm. All these features are observed to be partially filled with Fe and Mn. The Ca and P distribution is again found to vary considerably around the Haversian canal and the resorption cavity.

3.4. X-ray absorption fine structure

3.4.1. Strontium *K*-edge. The average local bonding of Sr in the cross section of the artiodactyl and perissodactyl bones was studied by means of Sr *K*-edge EXAFS spectroscopy. The macro EXAFS spectra detect all Sr phases existing in the probed depth of the samples. Spectra recorded at different areas in the cross section of each sample were identical in the XANES region and were added for better statistics. The Fourier transform (FT) amplitudes of the k^3-weighted $\chi(k)$ spectra are shown in Fig. 8. The spectra were fitted using the fluorapatite model, $Ca_5(PO_4)_3F$, where the central absorbing Ca atom was substituted by Sr. However, such a substitution was not taken into account for the fitting of the third and fourth nearest-neighbouring shells (SH3 and SH4) since the XRF measurements revealed that the Sr/Ca ratio in the samples was less than 10%. The fitting results of the average local environment of Sr in the samples are listed in Table 2.

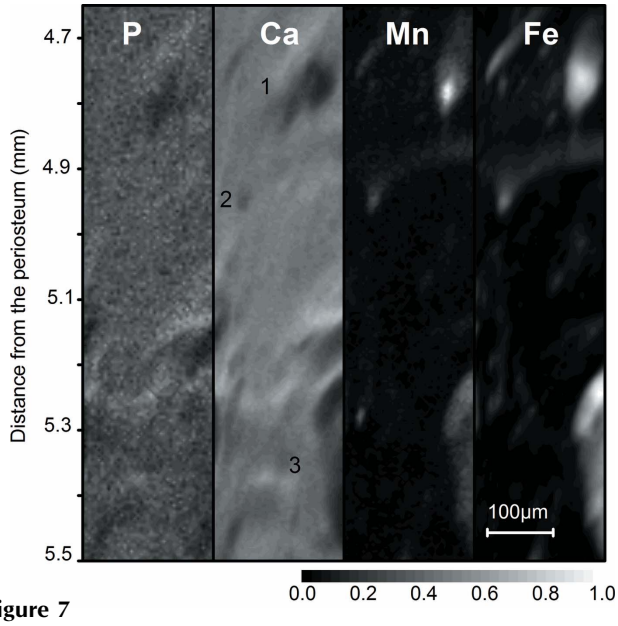

Figure 7
SR-XRF maps of the sample of the perissodactyl bone recorded at compact Haversian bone at a distance of approximately 5 mm from the periosteum. The incident beam impinges at 45° to the sample surface. The detector is positioned at right angles to the beam. The map of each element is normalized jointly with the corresponding map in Fig. 6 to the maximum of the element.

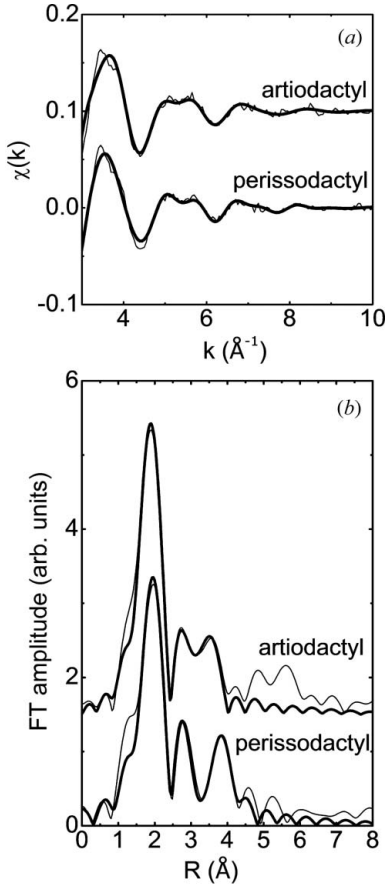

Figure 8
(*a*) Sr *K*-edge $\chi(k)$ and (*b*) corresponding amplitudes of the Fourier transforms of the $k^3\chi(k)$ spectra of the artiodactyl and the perissodactyl bone specimens. The experimental spectra and the fitting are shown by thin and thick lines, respectively.

The corresponding values for the Ca *K*-edge analysis of fluorapatite reported by Hughes *et al.* (1989) are also included in the table. Two available non-equivalent Ca sites (denoted as Ca_1 and Ca_2) exist in the unit cell of fluorapatite. In the Sr-fluorapatite model used, the three Sr—O nearest-neighbour distances for the Ca_1 site are 2.40, 2.46 and 2.81 Å with three oxygen atoms each. When Sr occupies the Ca_2 site, the Sr—O distances are 2.35, 2.37, 2.50 and 2.70 Å with two, one, two and one oxygen atoms, respectively. The average Sr—O bond distance is 2.55 and 2.46 Å, respectively, for the Ca_1 and Ca_2 sites. In the artiodactyl and perissodatyl bone, the average Sr—O distance was found equal to 2.49 ± 0.01 and 2.52 ± 0.01 Å, respectively, denoting substitutions in both Ca_1 and Ca_2 sites. The Sr *K*-edge EXAFS analysis results indicated that Sr substitutes for Ca in the apatite structure with no indication of Ca_1 or Ca_2 site preference.

3.4.2. Iron *K*-edge. The high concentration and spatial inhomogeneity of Fe in the studied artiodactyl and perissodactyl bones from the Milia excavation site dictate the investigation of the spatially resolved speciation of Fe. The Fe *K*-edge μ-XANES spectra of the artiodactyl and perissodactyl bones, recorded at Fe-rich and Fe-poor spots at the bone's cross sections, are shown in Fig. 9. The Fe *K*-edge macro-XANES spectra recorded at the artiodactyl bone cross section and the goethite reference sample are also included in the figure. Goethite (α-FeOOH) is the most abundant iron mineral phase in soils (Schwertmann & Taylor, 1989) and it is commonly present in fossil bones (Elorza *et al.*, 1999; Hubert *et al.*, 1996; Pfretzschner, 2001). The low-intensity peaks that appear below the Fe *K* absorption edge are related to $1s \rightarrow 3d$ transitions and shift to higher energies with the oxidation state of Fe (Srivastava & Nigam, 1973; White & McKinstry, 1966). More specifically, in Fe^{2+} and Fe^{3+} compounds the centroid of the pre-edge peak is located between 7112.0 and 7112.4 eV, and between 7113.4 and 7113.6 eV, respectively (Wilke *et al.*, 2001). Furthermore, the intensity of the pre-edge peak increases as the polyhedron around Fe becomes more distorted (or less centrosymmetric). In order to determine the centroid position and the integrated area under the pre-edge peaks, they were fitted using four Lorentzian components (L1–L4), as shown in the inset of Fig. 9. The fitting results are listed in Table 3. The L1 (7112.7 eV) and L2 (7114.1 eV) contributions are assigned to $1s \rightarrow 3d$ transitions related to the distorted polyhedron around Fe. The L3 (7115.6 eV) and L4 (7117.0 eV) contributions originate from the long-range interactions with 3*d* orbitals of Fe atoms in the second-nearest-neighbouring shell (Westre *et al.*, 1997; Wilke *et al.*, 2001) and their contribution is not included in the calculation

Table 3
Fitting results of the Fe *K*-edge pre-edge peak in the μ-XANES spectra of the artiodactyl and perissodactyl bone samples.

Four Lorentzian functions were used for the fitting: L1 (7112.7 eV), L2 (7114.1 eV), L3 (7115.6 eV) and L4 (7117.0 eV). The Fe/Ca and Mn/Fe weight ratios were determined from the XRF spectra recorded at the same spot.

Specimen	Fe/Ca	Mn/Fe	Pre-edge peak component	Area (arbitrary units)	Total area (arbitrary units)	Centroid position (eV)
Artiodactyl Fe-rich spot	2.3	–	L1	0.07	0.19	7113.6
			L2	0.12		
			L3	0.03		
			L4	0.03		
Artiodactyl Fe-poor spot	0.05	0.08	L1	0.05	0.13	7113.6
			L2	0.08		
			L3	0.01		
			L4	–		
Artiodactyl macro	0.14	0.02	L1	0.09	0.18	7113.4
			L2	0.09		
			L3	0.02		
			L4	0.01		
Perissodactyl Fe-rich spot	0.2	0.1	L1	0.09	0.2	7113.5
			L2	0.11		
			L3	0.04		
			L4	–		
Perissodactyl Fe-poor spot	0.07	0.12	L1	0.01	0.12	7114.0
			L2	0.11		
			L3	0.03		
			L4	–		
Goethite	–	–	L1	0.09	0.19	7113.4
			L2	0.10		
			L3	0.04		
			L4	0.04		

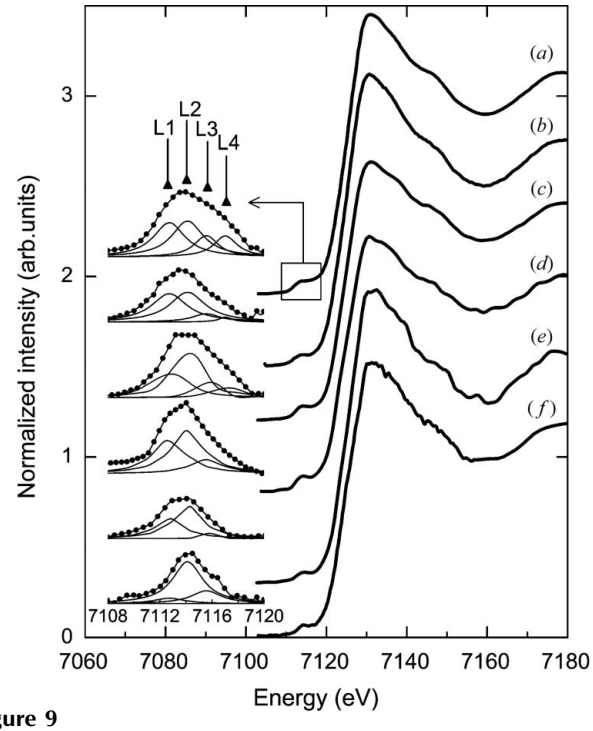

Figure 9
Fe *K*-edge μ-XANES spectra recorded at the cross sections of the artiodactyl [(*c*) Fe-rich spot, (*e*) Fe-poor spot] and perissodactyl [(*d*) Fe-rich spot, (*f*) Fe-poor spot] bones. A macro-XANES spectrum (*b*) of the artiodactyl specimen recorded at the centre of the cross section and the goethite reference (*a*) are also included. The fitting of the pre-edge peaks using four Lorentzian functions is shown in the inset.

of the centroid position in Table 3. The centroid positions in the experimental spectra range from 7113.4 to 7114.0 eV revealing that Fe is trivalent as in the case of iron (hydroxy)oxides (FeOOH), such as goethite. Fe in goethite is sixfold-coordinated forming slightly distorted octahedra. The area of the pre-edge peaks in the spectra recorded at Fe-rich spots and in the macro-XANES spectrum is consistent with that of goethite. The spectra recorded at Fe-poor spots in both samples exhibit a slightly smaller pre-edge peak area, revealing that the octahedron around Fe is slightly less distorted. It should also be noted that although the Fe/Ca ratio differs significantly among the Fe-rich and Fe-poor spots (the corresponding values are also listed in Table 3), the μ-XANES spectra are similar, indicating that the local environment of Fe is not significantly affected by its concentration. The formation of sub-micrometre- and micrometre-range Fe (hydroxy)oxide precipitates in fossil teeth due to diagenesis has been also previously reported (Kohn *et al.*, 1999).

Table 4
Fitting results of the Fe *K*-edge μ-EXAFS spectra recorded at the cross section of the artiodactyl and the perissodactyl bone.

The results of a macro EXAFS spectrum recorded at the cross section of the artiodactyl bone and a goethite reference are also included. *N* is the coordination number, *R* is the distance from the Fe absorbing atom, σ^2 is the Debye–Waller factor. During the iterations the value of *N* was kept fixed according to the model of the goethite reference.

		Nearest-neighbouring shells			
Specimen	Parameters	SH1: O	SH2: Fe (edge)	SH3: Fe (corner)	SH4: O
Artiodactyl	*N*	6	4	4	10
Fe-rich	*R* (Å)	1.98 ± 0.01	3.01 ± 0.01	3.49 ± 0.03	3.78 ± 0.04
spot	$\sigma^2 \times 10^{-3}$ (Å^2)	11	10	13	13
Artiodactyl	*N*	6	4	4	10
Fe-poor	*R* (Å)	1.99 ± 0.01	3.01 ± 0.03	3.49 ± 0.05	3.79 ± 0.09
spot	$\sigma^2 \times 10^{-3}$ (Å^2)	9	10	9	21
Artiodactyl	*N*	6	4	4	10
macro	*R* (Å)	2.00 ± 0.01	3.03 ± 0.01	3.43 ± 0.03	3.80 ± 0.04
	$\sigma^2 \times 10^{-3}$ (Å^2)	8	7	13	12
Perissodactyl	*N*	6	4	4	10
Fe-rich	*R* (Å)	1.99 ± 0.02	3.04 ± 0.03	3.46 ± 0.04	3.73 ± 0.08
spot	$\sigma^2 \times 10^{-3}$ (Å^2)	7	10	11	17
Goethite	*N*	6	4	4	10
	R (Å)	2.01 ± 0.01	3.04 ± 0.01	3.44 ± 0.02	3.80 ± 0.04
	$\sigma^2 \times 10^{-3}$ (Å^2)	9	8	11	12

The FT of the Fe *K*-edge EXAFS spectra of the artiodactyl bone (Fe-rich spot, Fe-poor spot, macro-EXAFS), the perissodactyl bone (Fe-rich spot) and the spectrum of the goethite reference sample are shown in Fig. 10. The spectra were fitted using the photoelectron scattering paths of goethite. During the fitting, the coordination numbers and the energy origin (ΔE_0) of the spectra of the bone specimens were kept fixed according to the goethite model whereas the rest of the parameters were allowed to vary. The fitting results are listed in Table 4. The first-nearest-neighbouring shell (SH1) in goethite is located at 2.01 Å and consists of six oxygen atoms. Although the octahedron around Fe is distorted, the individual Fe—O distances in the SH1 shell cannot be resolved by EXAFS. The respective Fe—O distances in the artiodactyl and perissodactyl bones are in agreement with the used structural model thus verifying the octahedral coordination of Fe. The SH2 and SH3 shells correspond to Fe—Fe distances of edge- and corner-sharing FeO_6 octahedra, respectively. These distances were found in agreement with the goethite model. Thus, both the Fe *K*-edge XANES and EXAFS analysis reveal the formation of Fe precipitates that adopt the structure of goethite, even though the Fe concentration varies significantly throughout the bone's cross section. Finally, incorporation of Fe in the apatite matrix does not take place in detectable amounts.

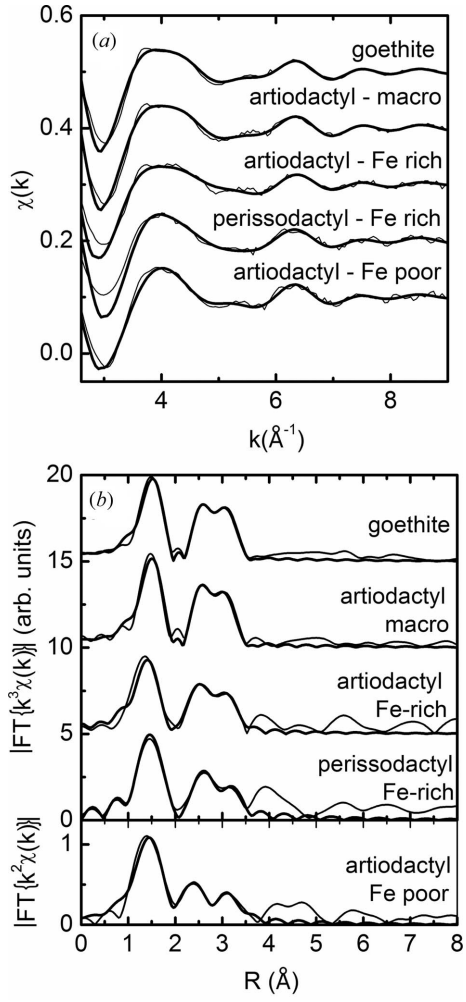

Figure 10
(*a*) Fe *K*-edge $\chi(k)$ and (*b*) corresponding amplitudes of the Fourier transforms of the k^n-weighted $\chi(k)$ spectra of the artiodactyl and perissodactyl bone specimens. The spectrum of the goethite reference is also included. The experimental spectra and the fitting curves are shown by thin and thick lines, respectively.

4. Conclusions

A histological, chemical and micro-structural characterization of the diagenetic alterations of artiodactyl and perissodactyl fossil bone fragments of the Earlymost Villafrancian was performed by means of optical light microscopy, scanning

electron microscopy and SR X-ray absorption and fluorescence spectroscopies. Optical light microscopy revealed that both bones are histologically well preserved. The perissodactyl cortex consists of compact Haversian bone while the artiodactyl bone is mainly fibro-lamellar with primary osteons arranged in a laminar to plexiform pattern. The SEM–BSE images have shown the presence of bacterial bores with diameter of 8 μm filled with spherical nodules in the periosteal area of the artiodactyl bone. Fe and Mn are the dominant contaminants in both bones forming aggregates in voids or precipitating along cracks. Linear XRF scans in the artiodactyl bone cross section revealed that the primary contamination path for soil-originating elements such as Fe and Mn was the periosteum and the medullar cavity. Local variations in the distribution of the apatite-related elements, and localization of metallic elements in the two different types of bone, were identified by two-dimensional XRF maps. The surrounding surfaces of the vascular canals and resorption cavities were found enriched in Ca and P. Based on the histological analysis and the metallic phases identified, high pH values governed the fossilization process during early and late diagenesis stages. The fluvial Plio-Pleistocene formation in which the fossils were found as well as collagen decay were the sources of sulfide resulting in the formation of pyrite that was detected in the form of small inclusions throughout the samples' cross sections by means of metallographic microscopy. Pyrite oxidation or pyrite decay is a crucial problem for the conservation of fossil specimens. In the presence of oxygen and water, ferrous sulfate ($FeSO_4$), sulfur dioxide (SO_2) and sulfuric acid (H_2SO_4) are produced which can cause great damage and even complete destruction of the specimens. Careful preparation of the fossils and controlled humidity conditions must be applied. The use of Paraloid, a common adhesive used to internally support fossils, is not adequate in this case. Sr *K*-edge EXAFS confirmed the incorporation of Sr in the bioapatite structure without obvious Ca site preference. The formation of goethite in the samples was identified with micro- and macro-Fe *K*-edge XAFS spectra even in positions where the Fe/Ca ratio varies significantly.

The measurements at the electron storage ring BESSY II of the Helmholtz Zentrum Berlin and HASYLAB-DESY were financially supported by the European Community's Seventh Framework Program (FP7/2007-2013) under grant agreement No. 226716. We would also like to thank Professor A. Erko for assistance during the measurements at the BESSY KMC-II beamline.

References

Ankudinov, A. L., Ravel, B., Rehr, J. J. & Conradson, S. D. (1998). *Phys. Rev. B*, **58**, 7565–7576.
Bandyopadhyay, P. & Segre, C. U. (undated). *Mucal on the web*, http://www.csrri.iit.edu/mucal.html.
Bartoll, J., Röhrs, S., Erko, A., Firsov, A., Bjeoumikhov, A. & Langhoff, N. (2004). *Spectrochim. Acta B*, **59**, 1587–1592.
Beck, L. A. (1985). *J. Hum. Evol.* **14**, 493–502.
Behrensmeyer, A. K., Western, D. & Dechant Boaz, D. E. (1979). *Paleobiology*, **5**, 12–21.
Bigi, A., Boanini, E., Capuccini, C. & Gazzano, M. (2007). *Inorg. Chim. Acta*, **360**, 1009–1016.
Boivin, G., Deloffre, P., Perrat, B., Panczer, G., Boudeulle, M., Mauras, Y., Allain, P., Tsouderos, Y. & Meunier, P. J. (1996). *J. Bone Miner. Res.* **11**, 1302–1311.
Child, A. M. (1995). *J. Archaeol. Sci.* **22**, 165–174.
Clarke, J. B. (1994). *Geol. Curator*, **6**, 11–15.
Collins, M. J., Nielsen-Marsh, C. M., Hiller, J., Smith, C. I., Roberts, J. P., Prigodich, R. V., Wess, T. J., Csapò, J., Millard, A. R. & Turner-Walker, G. (2002). *Archaeometry*, **44**, 383–394.
Cuijpers, A. G. F. M. (2006). *Int. J. Osteoarcheol.* **16**, 465–480.
Currey, J. D. (2002). *Bones: Structure and Mechanics*, 1st ed. New Jersey: Princeton University Press.
Curtin, A. J., Macdowell, A. A., Schaible, E. G. & Roth, V. L. (2012). *J. Vert. Paleontol.* **32**, 939–955.
Dumont, M., Zoeger, N., Streli, C., Wobrauschek, P., Falkenberg, G., Sander, P. M. & Pyzalla, A. R. (2009). *Powder Diffr.* **24**, 130–134.
Elliott, J. C., Wilson, R. M. & Dowker, S. E. P. (2002). *Adv. X-ray Anal.* **45**, 172–181.
Elorza, J., Astibia, H., Murelaga, X., Pereda-Superbiola, X. (1999). *Cretac. Res.* **20**, 169–187.
Enlow, D. H. & Brown, S. O. (1956). *Tex. J. Sci.* **8**, 405–443.
Enlow, D. H. & Brown, S. O. (1958). *Tex. J. Sci.* **10**, 187–230.
Ezzo, J. A. (1994*a*). *Am. Antiq.* **59**, 606–621.
Ezzo, J. A. (1994*b*). *J. Anthropol. Archaeol.* **13**, 1–34.
Gilbert, R. (1975). PhD dissertation, University of Massachusetts, USA.
Gingerich, P. D. (1984). *Am. J. Phys. Anthropol.* **27**, 57–72.
Gruner, J. W. & McConnell, D. (1937). *Z. Kristallogr.* **97**, 208–215.
Guggenheim, K. & Gaster, D. (1973). *Biological Mineralization*, edited by I. Zipkin, pp. 443–462. New York: John Wiley.
Frank-Kamenetskaya, O. V. (2008). *Minerals as Advanced Materials I*, edited by S. Krivovichev, pp. 241–252. Berlin: Springer.
Hackett, C. J. (1981). *Med. Sci. Law*, **21**, 243–265.
Hedges, R. E. M., Millard, A. R. & Pike, A. W. G. (1995). *J. Archaeol. Sci.* **22**, 201–209.
Hiller, J. C. & Wess, T. J. (2006). *J. Archaeol. Sci.* **33**, 560–572.
Hubert, J. F., Panish, P. T., Chure, D. J. & Prostak, K. S. (1996). *J. Sediment. Res.* **66**, 531–547.
Hughes, J. M., Cameron, M. & Crowley, K. D. (1989). *Am. Mineral.* **74**, 870–876.
Hughes, J. M., Cameron, M. & Crowley, K. D. (1991). *Am. Mineral.* **76**, 1857–1862.
İzci, Y., Kaya, S., Erdem, O., Akay, C., Kural, C., Soykut, B., Başoğlu, O., Şenyurt, Y., Kılıç, S. & Temiz, Ç. (2013). *J. Anthropol.* **2013**, 534186.
Janssens, K. H. A., Adams, F. C. V. & Rindby, A. (2000). *Microscopic X-ray Fluorescence Analysis.* Chichester: Wiley.
Kohn, M. J., Schoeninger, M. J. & Barker, W. W. (1999). *Geochim. Cosmochim. Acta*, **63**, 2737–2747.
Lambert, J. B., Szpunar, C. B. & Buikstra, J. E. (1979). *Archaeometry*, **21**, 115–129.
Lambert, J. B., Simpson, S. V., Szpunar, C. B. & Buikstra, J. E. (1984). *Acc. Chem. Res.* **17**, 298–305.
Lambert, J. B., Vlasak Simpson, S., Szpunar, C. B. & Buikstra, J. E. (1985). *J. Hum. Evol.* **14**, 477–482.
Lambert, J. B., Vlasak Simpson, S., Thometz, A. C. & Buikstra, J. E. (1982). *Am. J. Phys. Anthropol.* **59**, 289–294.
Lebon, M., Müller, K., Bahain, J. J., Fröhlich, F., Falguères, C., Bertrand, L., Sandt, C. & Reiche, I. (2011). *J. Anal. At. Spectrom.* **26**, 922–929.
Li, Z. Y., Lam, W. M., Yang, C., Xu, B., Ni, G. X., Abbah, S. A., Cheung, K. M. C., Luk, K. D. K. & Lu, W. W. (2007). *Biomaterials*, **28**, 1452–1460.
Marchiafava, V., Bonucci, E. & Ascenzi, A. (1974). *Calcif. Tissue Res.* **14**, 195–210.

Martiniakovà, M., Grosskopf, B., Omelka, R., Vondráková, M. & Bauerová, M. (2006). *J. Forensic Sci.* **51**, 1235–1239.
Mazurier, A., Volpato, V. & Macchiarelli, R. (2006). *Appl. Phys. A*, **83**, 229–233.
Mehmel, M. (1930). *Z. Kristallogr.* **75**, 323–331.
Newesely, H. (1989). *Appl. Geochem.* **4**, 233–245.
Newville, M., Ravel, B., Haskel, D., Rehr, J. J., Stern, E. A. & Yacoby, Y. (1995). *Physica B*, **208**–**209**, 154–156.
Nicholson, R. A. (1996). *J. Archaeol. Sci.* **23**, 513–533.
Pasero, M., Kampf, A. R., Ferraris, C., Pekov, I. V., Rakovan, J. & White, T. J. (2010). *Eur. J. Mineral.* **22**, 163–179.
Pfretzschner, H. U. (2001). *N. Jahrb. Geol. Paläont. Abh.* **220**, 417–429.
Pfretzschner, H. U. (2004). *C. R. Palevol.* **3**, 605–615.
Ravel, B. & Newville, M. (2005). *J. Synchrotron Rad.* **12**, 537–541.
Reiche, I., Lebon, M., Chadefaux, C., Müller, K., Le Hô, A.-S., Gensch, M. & Schade, U. (2010). *Anal. Bioanal. Chem.* **397**, 2491–2499.
Ricqles, A. J. de (1975). *Ann. Paleont.* **61**, 51–129.
Ricqles, A. J. de, Meunier, F. J., Castanet, J. & Fracillon-Vieillot, H. (1991). *Bone: Bone Matrix and Bone Specific Products*, Vol. 2, edited by B. K. Hall. London: CRC Press.
Rochefort, G. Y., Pallu, S. & Benhamou, C. L. (2010). *Osteoporosis Int.* **21**, 1457–1469.
Rogoz, A., Sawlowicz, Z. & Wojtal, P. (2012). *Palaios*, **27**, 541–549.
Roschger, P., Manjubala, I., Zoeger, N., Meirer, F., Simon, R., Li, C., Fratzl-Zelman, N., Misof, B. M., Paschalis, E. P., Streli, C., Fratzl, P. & Klaushofer, K. (2010). *J. Bone Miner. Res.* **25**, 891–900.
Rousseau, R. M. (1984). *X-ray Spectrom.* **13**, 115–120.
Safont, S., Malgosa, A., Subirà, M. E. & Gibert, J. (1998). *Int. J. Osteoarchaeol.* **8**, 23–37.
Sasowsky, I. D. & Mylroie, J. (2007). *Studies of Cave Sediments: Physical and Chemical Records of Paleoclimate*, 2nd ed. Dordrecht: Springer.
Schutkowski, H., Herrmann, B., Wiedemann, F., Bocherens, H. & Grupe, G. (1999). *J. Archaeol. Sci.* **26**, 675–685.
Schwertmann, U. & Taylor, R. M. (1989). *Minerals in Soil Environments*, edited by J. B. Dixon and S. B. Weed, 2nd ed., pp. 379–438, Madison: Soil Science Society of America.
Sheldon, N. D. & Tabor, N. J. (2009). *Earth Sci. Rev.* **95**, 1–52.
Skinner, H. C. W. (2005). *Medical Geology*, edited by O. Selenus, ch. 28. New York: Elsevier.
Srivastava, U. C. & Nigam, H. L. (1973). *Coordin. Chem. Rev.* **9**, 275–310.
Tamm, T. & Peld, M. (2006). *J. Solid State Chem.* **179**, 1581–1587.
Terra, J., Dourado, E. R., Eon, J. -G., Ellis, D. E., Gonzalez, G. & Rossi, A. M. (2009). *Phys. Chem. Chem. Phys.* **11**, 568–577.
Tsoukala, E. (2000). *Ann. Paleontol.* **86**, 165–191.
Tsoukala, E. & Lister, A. (1998). *Boll. Soc. Paleont. Ital.* **37**, 117–139.
Vekemans, B., Janssens, K., Vincze, L., Adams, F. & Van Espen, P. (1994). *X-ray Spectrom.* **23**, 278–285.
Von Endt, D. W. & Ortner, D. J. (1984). *J. Archaeol. Sci.* **11**, 247–253.
Wedl, C. (1864). *Akad. Wiss. Wien Math. Naturwiss. Kl. (I)*, **50**, 171–193.
Wess, T., Alberts, I., Hiller, J., Drakopoulos, M., Chamberlain, A. T. & Collins, M. (2001). *Calcif. Tissue Int.* **70**, 103–110.
Westre, T. E., Kennepohl, P., DeWitt, J. G., Hedman, B., Hodgson, K. O. & Solomon, E. I. (1997). *J. Am. Chem. Soc.* **119**, 6297–6314.
White, C. D. & Schwarcz, H. P. (1989). *J. Archaeol. Sci.* **16**, 451–474.
White, E. H. & McKinstry, H. A. (1966). *Adv. X-ray Anal.* **9**, 376–392.
White, E. M. & Hannus, L. A. (1983). *Am. Antiq.* **48**, 316–322.
Wilke, M., Farges, F., Petit, P.-E., Brown, G. E. Jr & Martin, F. (2001). *Am. Mineral.* **86**, 714–730.
Wings, O. (2004). *Palaeogeogr. Palaeoecl.* **204**, 15–32.
Wopenka, B. & Pasteris, J. D. (2005). *Mater. Sci. Eng. C*, **25**, 131–143.